RSC Advances

PAPER

View Article Online
View Journal | View Issue

Cite this: *RSC Adv.*, 2022, **12**, 30803

A crystal defect led zero thermal quenching β-$NaYF_4:Eu^{3+},Dy^{3+}$ red emitting phosphor†

Shaokun Ling,[b] Chang Chen,[b] Kai Meng,[b] Yifeng Yan,[b] Junyun Ming,[b] Sen Liao *[ab] and Yingheng Huang*[b]

Received 8th September 2022
Accepted 28th September 2022

DOI: 10.1039/d2ra05674g

rsc.li/rsc-advances

Red-light phosphors with extraordinary and stable thermal luminous properties must urgently be explored under the circumstances that commercial phosphors are suffering from serious thermal quenching effects and a lack of red-light components. Synthesized by a one-step hydrothermal method, a new type of $NaYF_4:0.065Eu^{3+},0.003Dy^{3+}$ phosphor with notable thermal luminous stability is reported in this study. As well as energy transfer between Dy^{3+} and Eu^{3+}, this novel red-light phosphor manifests zero thermal quenching (ZTQ) performance under an increasing temperature of measurement. The ZTQ property stems from the interior defects of the crystal produced by the non-equivalence replacement between distinct ions. Density Functional Theory (DFT) calculations were utilized to verify the formation energy of two kinds of defects that make a vital contribution to the ZTQ performance of the $NaYF_4:0.065Eu^{3+},0.003Dy^{3+}$ phosphor. This finding could make some contributions towards research into improving thermal luminous properties and stability.

1. Introduction

Since the birth of the commercial light emitting diode (LED) in 1968, LEDs have been applied in various fields due to its merits of being energy saving and environmentally friendly[1–3] such as basic illumination,[4] cultivation of plants,[5,6] indoor illumination in hospitals for physical health care,[7] and as a backlight source for large scale LCDs.[8,9] The WLED is the most important and famous application of LEDs and is used in various application fields. Up to now, it is the most successful method that combines a $YAG:Ce^{3+}$ yellow emitting phosphor with a blue-light emitting semiconductor InGaN chip to obtain white light.[10,11] However, current commercial WLEDs illumination systems suffer from a shortage of high correlated color temperatures (CCTs) and low color rendering indexes (CRIs) due to the deficiency of red-light components.[12,13] $YAG:Ce^{3+}$ phosphors present serious quenching of luminous intensity at high operating temperatures,[14–16] which diminishes the luminous properties of WLEDs. To overcome these shortcomings, research into stable and reliable red-light performance is prompted by the shortage of current commercial WLEDs.

Eu^{2+} doped nitride-based red phosphors provide a new approach to resolve the problem of a lack of a red-light source with high chemical and luminous stability for WLEDs. $Sr[LiAl_3N_4]:Eu^{2+}$ was reported as a novel type of red phosphor with zero thermal quenching red light emitting property in a temperature range from 300 K to 600 K.[17] Other researchers have reported that $Li_2CaSi_2N_4$ based phosphors present zero thermal quenching and color tunable properties.[18] These reports indicate that nitride-based phosphors have an enormous potential to be an ideal matrix for red-light emission phosphors. Unfortunately, the major obstacle limiting further application of nitride-based red-light phosphors is high synthesis costs induced by the rigorous synthesis condition that require high synthetic temperature and purity of atmosphere. To successfully synthesize nitride-based phosphors, it is necessary to keep the raw materials in a highly pure N_2 atmosphere. For example, $Sr[LiAl_3N_4]:Eu^{2+}$ was synthesized in a mixed atmosphere ($N_2:H_2 = 95:5$) at 1000 °C and lasted for 2 hours.[17] $Li_2CaSi_2N_4$ was prepared in a 0.4 MPa N_2 atmosphere heated to 1000 °C and lasted for 4 hours.[18]

The trivalent europium ion, Eu^{3+}, is considered as an ideal red-light source, due to its extraordinary red photoluminescence performance in inorganic substrates.[19] Furthermore, Eu^{3+} red-light luminous materials, such as $Y_2O_2S:Eu^{3+}$ and $Y_2O_3:Eu^{3+}$, have been commercialized in LEDs and are the most well-known and successful red-light sources. Unfortunately, $Y_2O_3:Eu^{3+}$ phosphors suffer from serious thermal quenching that diminishes the luminous performance with increasing temperature.[20] Furthermore, $Y_2O_2S:Eu^{3+}$ phosphors may decompose and release sulfides.[21] This sulfide will not only

[a]School of Chemistry and Chemical Engineering, Guangxi University, Nanning, Guangxi, 530004, China. E-mail: liaosen@gxu.edu.cn; liaosen380@sina.com; Fax: +86 771 3233718; Tel: +86 771 3233718

[b]School of Resources, Environment and Materials, Guangxi University, Nanning, Guangxi, 530004, China. E-mail: huangyingheng@163.com; lsk0708@163.com; 249443176@qq.com; 1006779688@qq.com; 1024487385@qq.com; 2945539376@qq.com

† Electronic supplementary information (ESI) available. See DOI: https://doi.org/10.1039/d2ra05674g

lead to degeneration of luminous properties, but may also have a harmful effect on human health. These fatal defects constrain the utilization of $Y_2O_2S:Eu^{3+}$ and $Y_2O_3:Eu^{3+}$ red-light phosphors. It is urgent to synthesize a novel type of host material for red-light Eu^{3+} phosphors which possesses outstanding thermal luminous and chemical stability.

Fluorides, due to their superior chemical stability, low possibility of non-radiative transitions, and low phono energy, have a high potential as a matrix for luminescence ions. Mn^{4+}-doped fluoride phosphors, such as $K_2TiF_6:Mn^{4+}$ and $K_2SiF_6:Mn^{4+}$, were reported.[22,23] These phosphors also exhibit outstanding red-light properties. However, unfortunately, the synthesis of Mn^{4+}-doped fluoride phosphors utilize HF frequently, which inevitably could cause physical harm to the human body and is not suitable for commercial production. Most importantly, fluorides have superb compatibility for luminous lanthanide ions.[24–26] Possessing the various merits of fluorides, $NaYF_4$ is considered as one of the most suitable host materials for lanthanide luminous ions. As reported previously, Yb^{3+} and Er^{3+} co-doped $NaYF_4$ nanoparticles were employed to improve the accuracy of miRNA detection,[27] indicating selected chemical stability and safety of $NaYF_4$ for the human body. Unlike nitride-based phosphors, there are distinct synthesis strategies to obtain $NaYF_4$ phosphors with high chemical stability and luminous properties, such as electrospinning,[28] thermal decomposition,[29] co-precipitation,[30] and the hydrothermal method.[31,32] In these mentioned synthesis methods, the hydrothermal method is the most cost-effective synthesis compared with thermal decomposition and electrospinning. Moreover, the hydrothermal method has better safety and operational processes.[33] Compared with the co-precipitation method that synthesizes cubic $NaYF_4$ (α-$NaYF_4$), the hydrothermal method can obtain hexagonal $NaYF_4$ (β-$NaYF_4$) which possesses outstanding optical property compared to α-$NaYF_4$.

In this study, Eu^{3+} and Dy^{3+} were chosen as the activator and sensitizer, respectively. The energy transfer between Dy^{3+} and Eu^{3+} could occur due to the higher energy level of the $^4F_{9/2}$ of the Dy^{3+} ion compared to the $^5D_0$ and $^5D_1$ of the Eu^{3+} ion.[34–36] The existence of Dy^{3+} leads to an improvement of the red-light emitting properties for Eu^{3+}. A one-step hydrothermal method was utilized to synthesize a Eu^{3+} and Dy^{3+} co-doped hexagonal $NaYF_4$ phosphor with outstanding chemical stability and thermal luminous performance. DFT calculations were used to determine the factor responsible for the extraordinary thermal luminous properties, which is distinct from other Eu^{3+}-doped $NaYF_4$ phosphors[37,38] without intriguing thermal luminous properties. This study could make a contribution to tackling the problem of the lack of stable red-light components in high temperature working conditions.

2. Experimental

2.1 Experiment process

A series of $NaYF_4:0.065Eu^{3+},xDy^{3+}$ (x = 0, 0.001, 0.002, 0.003, 0.004, and 0.005) were synthesized by a one-step hydrothermal method. The details of the synthesis are as follows: (i) $NaNO_3$ (2 mol L^{-1}), $Y(NO_3)_3$ (1 mol L^{-1}), $Eu(NO_3)_3$ (1 mol L^{-1}), $Dy(NO_3)_3$ (1 mol L^{-1}), and NH_4F (6 mol L^{-1}) solutions were prepared. (ii) $NaNO_3$, $Y(NO_3)_3$, $Eu(NO_3)_3$, and $Dy(NO_3)_3$ solutions were mixed with a stoichiometric ratio of $1:(1-0.065-x):0.065:x$, corresponding to the ion ratio of $Na^+:Y^{3+}:Eu^{3+}:Dy^{3+}$ and named solution A. Solution A was stirred for 20 minutes inside Teflon containers. (iii) 10 ml NH_4F solution was added into solution A, which produced a white colloidal precursor. The mixture solution containing the precursor was continually stirred for 30 minutes. (iv) After even stirring, the Teflon containers with the mixed solution and precursors produced in step (iii) were inserted into the hydrothermal autoclave and heated to 230 °C. They lasted at this temperature for 72 hours. (v) The final products were washed several times and dried at 120 °C for 2 hours.

2.2 Characterization

The crystal structure of all samples was characterized by X-ray powder diffraction (Bruker D8). Refinement of the X-ray data was processed by the GSAS program. The morphology and energy disperse spectrometer of the sample were observed and detected by a scanning electron microscope from Hitachi (SU4800). High resolution transmission electron microscopy (HRTEM) and selected area electron diffraction were implemented by JEM-2100. To characterize the fluorescent performance, measurement of PL and PLE spectra, as well as the decay of the sample were implemented by a Horiba FluoroMax4 spectrophotometer. High temperature PL spectra and decay were measured on the same optical platform. ESCALAB-250+ X-ray photoelectron spectra were employed to analyze the elements and chemical bonds qualitatively. Crystal defects were characterized by electron paramagnetic resonance (EPR, Bruker EMXplus-6/1).

2.3 Calculations

The band structure, density of states, and formation energy of the crystal defects were calculated by the VASP program. The PAW-PBE and DFT+U methods were utilized for calculation of the band structure and density of states (DOS). The files VASP needed were prepared by VASPKIT.[39] The process for determining the formation energy of defects can be described as the following: (i) geometry optimization of a single cell was implemented. (ii) On the basis of the optimization of a single cell, a supercell with $2 \times 2 \times 2$ was built. (iii) Na and Y ions in a supercell were replaced by Y and Na ions, respectively. (iv) Geometry optimization for the whole system was implemented to find out the minimum energy.

3. Results and discussion

3.1 X-ray powder diffraction results

As illustrated in Fig. 1a, compared with the standard PDF card, the X-ray powder diffraction patterns of $NaYF_4:0.065Eu^{3+},xDy^{3+}$ (x = 0, 0.001, 0.002, 0.003, 0.004, and 0.005) are in good agreement with the diffraction peaks of PDF#28-1192 which represent the phase of $Na_{0.57}Y_{0.39}Yb_{0.06}ErF_4$. From the XRD patterns, impurity phases were not detected, which proved the

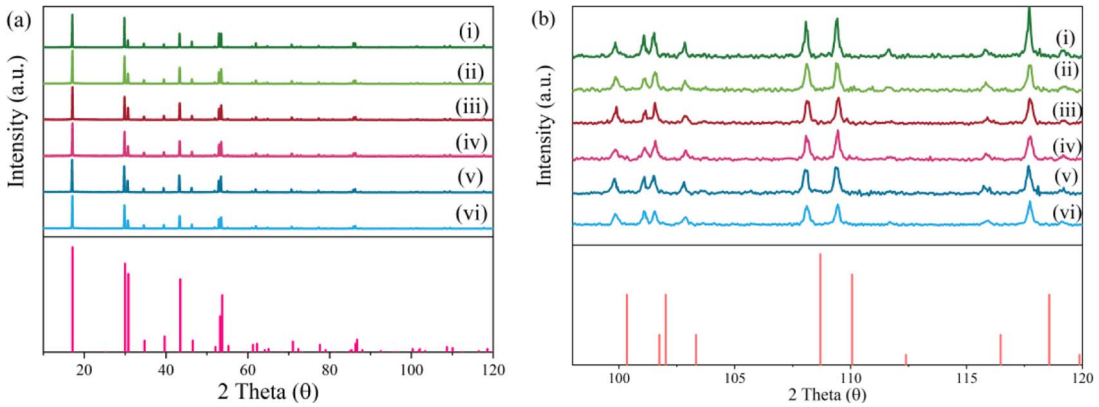

Fig. 1 X-ray patterns of the samples (i–vi) $NaYF_4$: $0.065Eu^{3+}$,xDy^{3+}((i–vi), x = 0.00, 0.001, 0.002, 0.003, 0.004, and 0.005). (a) Full patterns. (b) Local expanded patterns.

successful synthesis of a high purity single phase of a series of $NaYF_4$: $0.065Eu^{3+}$,xDy^{3+} samples. As shown in Fig. 1b, compared with the standard PDF card, between a 2 theta value from 92° to 120°, diffraction peaks of all samples present a slight skewing to lower angles due to the larger ion radius of Eu^{3+} and Dy^{3+} compared to Yb^{3+} and Er^{3+}.

3.2 Analysis of crystal morphology and elements

As illustrated in Fig. 2a–d, the morphology of $NaYF_4$: $0.065Eu^{3+}$,$0.003Dy^{3+}$ was observed by SEM at magnifications of 2.0 K, 3.0 K, 4.0 K, and 5.0 K, respectively. The sample was ground up with an agate mortar before observation. Crystal grains with an even prism shape and a smooth crystal grain surface were obtained. The size of the grains was detected to be 4 × 10 μm. From Fig. 2e–i, EDS mapping graphs of the sample indicate that all the elements Na, Y, F, Eu, Dy were uniformly dispersed in the crystal grains. Elements Eu and Dy were successfully incorporated into the β-$NaYF_4$ substrate.

The X-ray photoelectron spectrum of $NaYF_4$: $0.065Eu^{3+}$,$0.003Dy^{3+}$ is shown in Fig. 3a. Fig. 3b and c illustrate

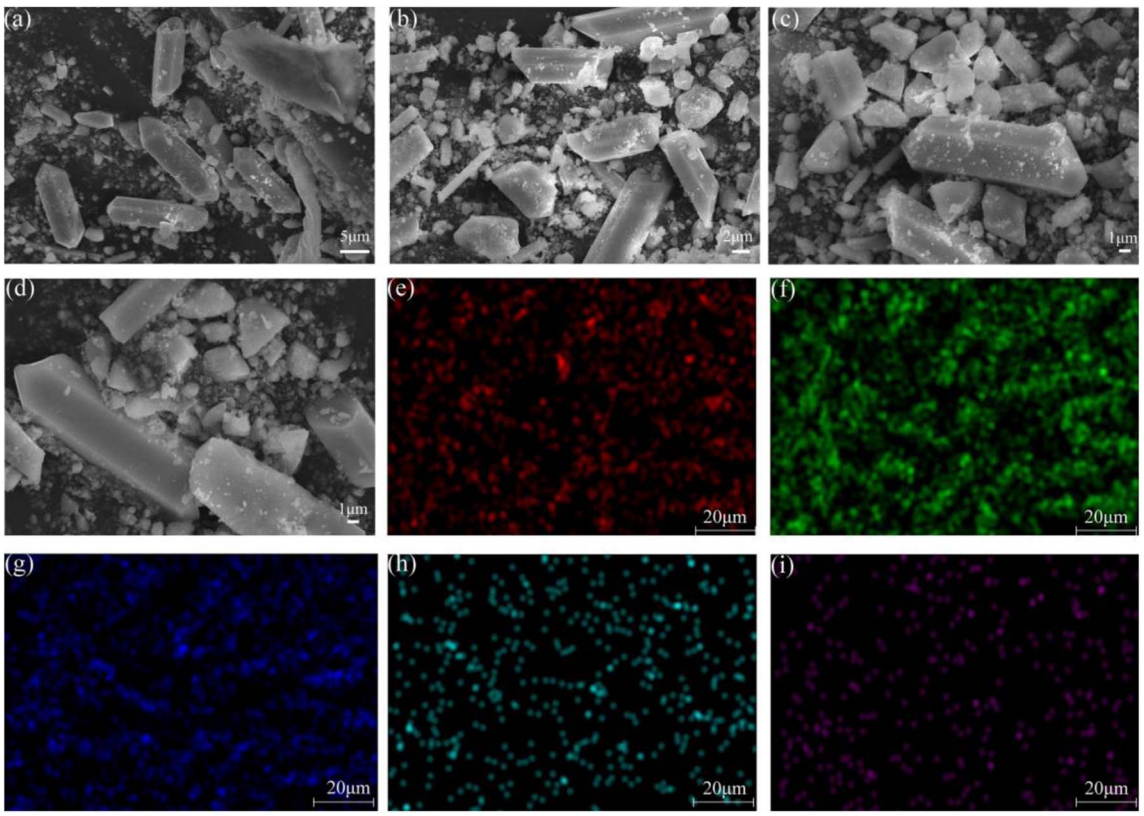

Fig. 2 SEM images observed at magnifications of (a) 2.0 K, (b) 3.0 K, (c) 4.0 K, and (d) 5.0 K. EDS mapping of (e) Na, (f) Y, (g) F, (h) Eu, and (i) Dy.

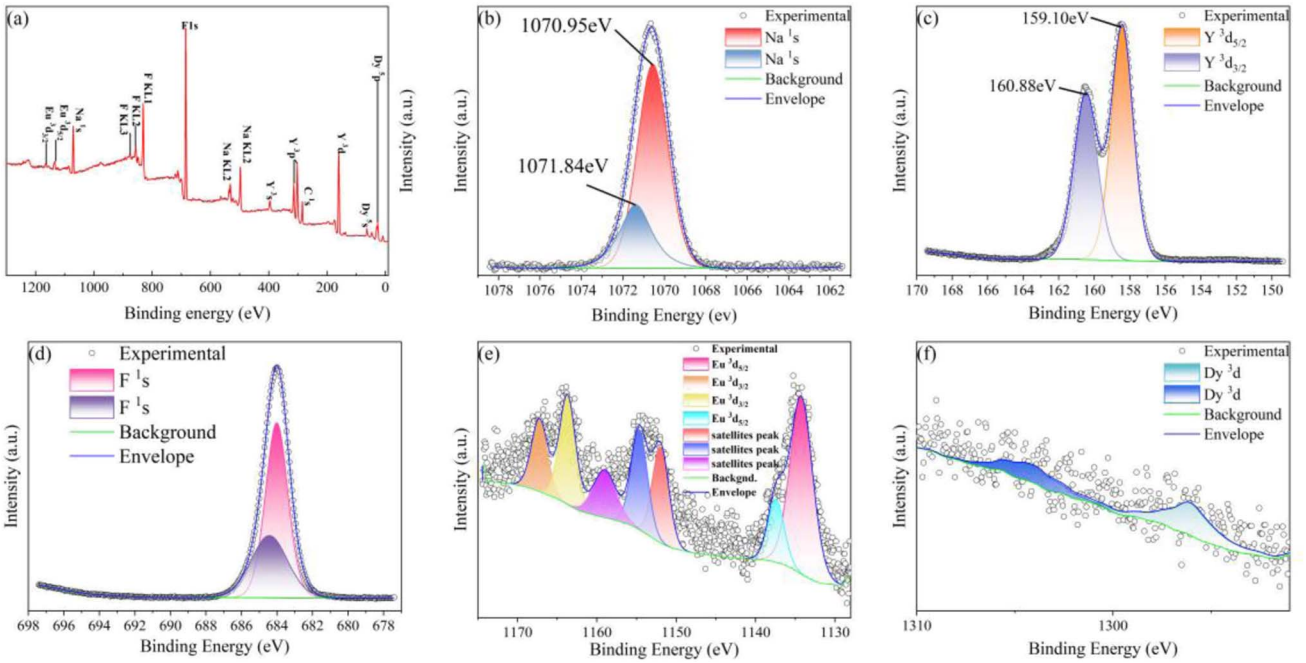

Fig. 3 (a) XPS survey spectrum of $NaYF_4$: $0.065Eu^{3+}$,$0.003Dy^{3+}$. High resolution spectra of (b) Na, (c) Y, (d) F, (e) Eu, and (f) Dy.

the high-resolution XPS spectra of Na^+ and Y^{3+}. Fig. 3e, the high-resolution XPS spectra of Eu^{3+}, presents two different peaks owing to the $5d_{5/2}$ energy level. The peak located at a binding energy of 1134.83 eV and 1138.03 eV demonstrated by the fitted result may be ascribed to the splitting of the $5d_{5/2}$ energy level. Satellites peaks were present at 1152.56 eV to 1159.60 eV. Finally, the binding energy located at 1164.30 eV and 1164.83 eV can be ascribed to the $3d_{3/2}$ energy level. Fig. 3f shows the high-resolution XPS spectra of Dy^{3+} and its fitted result, the fitted peaks at a binding energy of 1296.62 eV could be attributed to the $3d_{5/2}$ energy level, respectively. The XPS results further indicate that the Dy^{3+} ion was successfully incorporated into the $NaYF_4$ matrix.

3.3 TEM, X-ray refinement, and crystal structure

As demonstrated in Fig. 4a, the TEM graph of the crystal grain is shown. Graphs of HRTEM and SAED were obtained based on Fig. 4a. As illustrated in Fig. 4b, the graph of the HRTEM shows the distance of the crystal face of (100) and (110), corresponding to the crystal face distance of 0.506 Å and 0.279 Å. As illustrated in Fig. 4c, redundant light spots are not observed, indicating the pure phase of β-$NaYF_4$. Results of HRTEM and SAED were in good agreement with the XRD patterns which indicate the purity of phase. The diffraction spots of (100) and (110) were detected and shown in the SAED graph. The results of the HRTEM and SAED also provide reliable information on the X-ray refinement. The χ^2, R_{wp}, R_p, and R_{bragg} values of the X-ray diffraction refinement are equal to 1.892, 8.50%, 6.27%, and 6.29, respectively, which indicates an extraordinary fitness result and reliable information of the crystal structure. The refinement pattern of XRD is shown in Fig. 4d, which is consistent with the experimental data.

Combining the X-ray diffraction data and GSAS program, the crystal information of the $NaYF_4$: $0.065Eu^{3+}$,$0.003Dy^{3+}$ sample was obtained and is listed in Table 1. The result of the refinement indicates that the crystal system and space group of the sample are hexagonal and $P6_3/m$ (176), respectively. Due to the relatively low Dy^{3+} concentration, the Dy^{3+} ion was not taken into consideration due to the few contributions to the XRD pattern. Na and Y atoms exist at two distinct positions in the β-$NaYF_4$: $0.065Eu^{3+}$ structure. In the coordinate value (0.0, 0.0, 0.11413), Na and Y occupy an equivalent position, named Na1 and Y2, respectively. Similarly, at a position for which the coordinate value is (0.6667, 0.3333, 0.25), the Y and Na atoms occupy an equivalent atom position, labelled Y1 and Na2, respectively.

As shown in Fig. 5a–e, the crystal structure of β-$NaYF_4$: $0.065Eu^{3+}$,$0.003Dy^{3+}$ was portrayed by the Diamon-3 program. Watching the structure from the perspective parallel to the connection line of the vertex of the a and c axis, the integrated crystal structure is constituted of Na–F octahedron and Y–F decahedron. Named $[YF_8]$, the Y–F decahedron is composed of a Y atom and nine F atoms, as depicted in Fig. 5b. Consisting of two central Na atoms and six F atoms, the Na–F octahedron is named as $[Na_2F_6]$, as illustrated in Fig. 5c. Noticeably, the $[YF_8]$ decahedrons and $[Na_2F_6]$ octahedron occupy the centre of the crystal cell and the edge line parallel to the direction of the connected line between a and c axis. Fig. 5d illustrates the process by which Eu^{3+} and Dy^{3+} ions replace the Y^{3+} inside the $[YF_8]$ decahedron.

To obtain the energy gap of β-$NaYF_4$, ultraviolet absorption spectroscopy was employed. The ultraviolet absorption spectra and photo energy spectra of β-$NaYF_4$ are shown in Fig. 5d. The energy gap is calculated by eqn (1):

$$(\alpha h\nu)^n = A(h\nu - E_g) \quad (1)$$

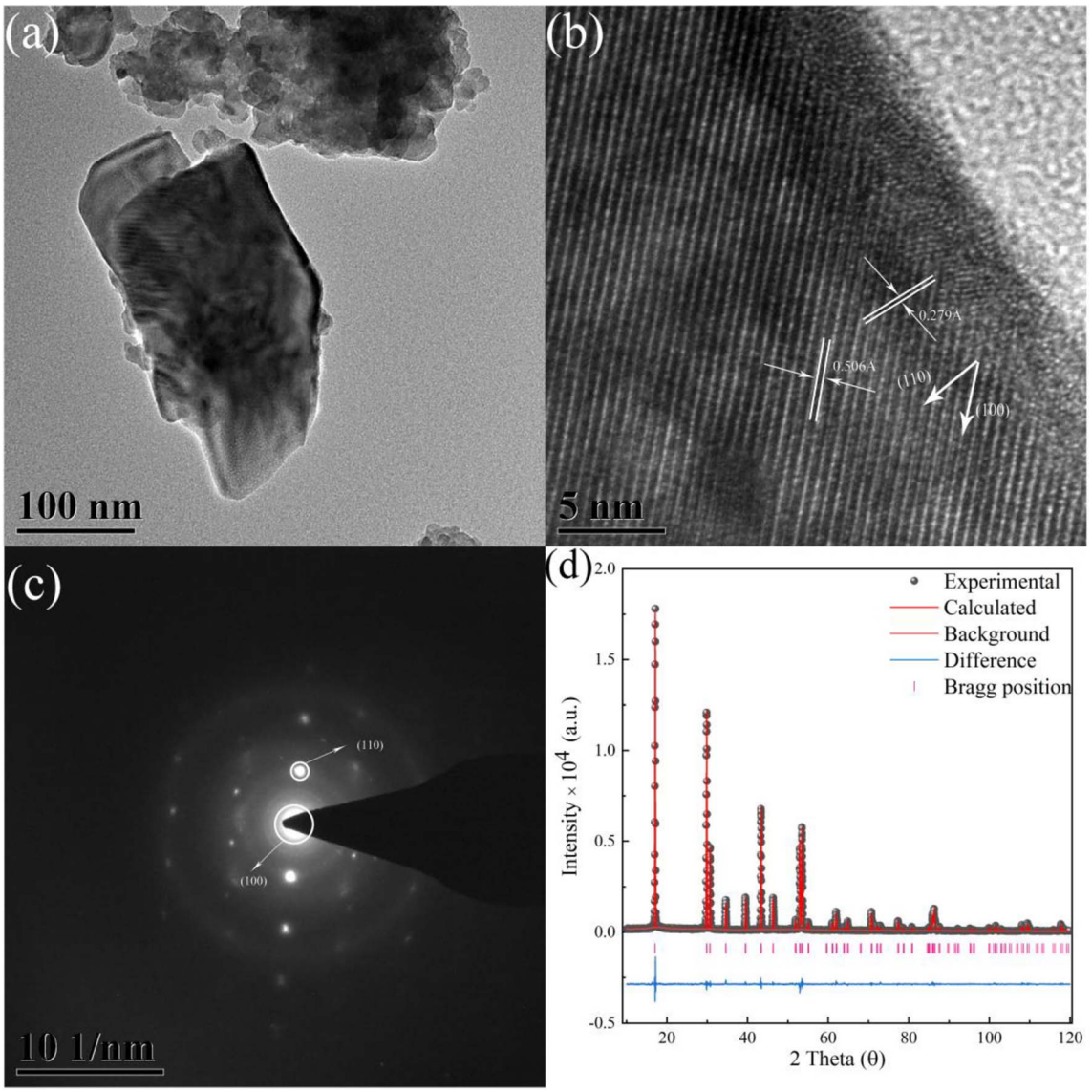

Fig. 4 (a) The TEM graph of $NaYF_4$: $0.065Eu^{3+}$,$0.003Dy^{3+}$. (b) The HRTEM graph of the sample. (c) The SAED graph of the sample. (d) The X-ray refinement pattern of $NaYF_4$: $0.065Eu^{3+}$,$0.003Dy^{3+}$.

Table 1 The results of the Rietveld refinement of β-NaYF4 : $0.065Eu^{3+}$

Formula sum	β-$Na(0.935Y)F_4$: $0.065Eu^{3+}$		
Formula weight	191.9889		
Crystal system	Hexagonal		
Space group	$P6_3/m$ (176)		
Cell parameters	$a = 5.985309(27)$ Å	$b = 5.984911$ Å	$c = 3.52072(5)$ Å
Cell volume	109.212(20)		
Z	6		
Atom	x/a	y/b	z/c
Na1	0.0	0.0	0.11413(10)
Na2	0.6667	0.3333	0.25
Y1	0.6667	0.3333	0.25
Y2	0.0	0.0	0.11413(10)
Eu1	0.6667	0.3333	0.25
F1	0.3090(4)	0.2795(4)	0.25

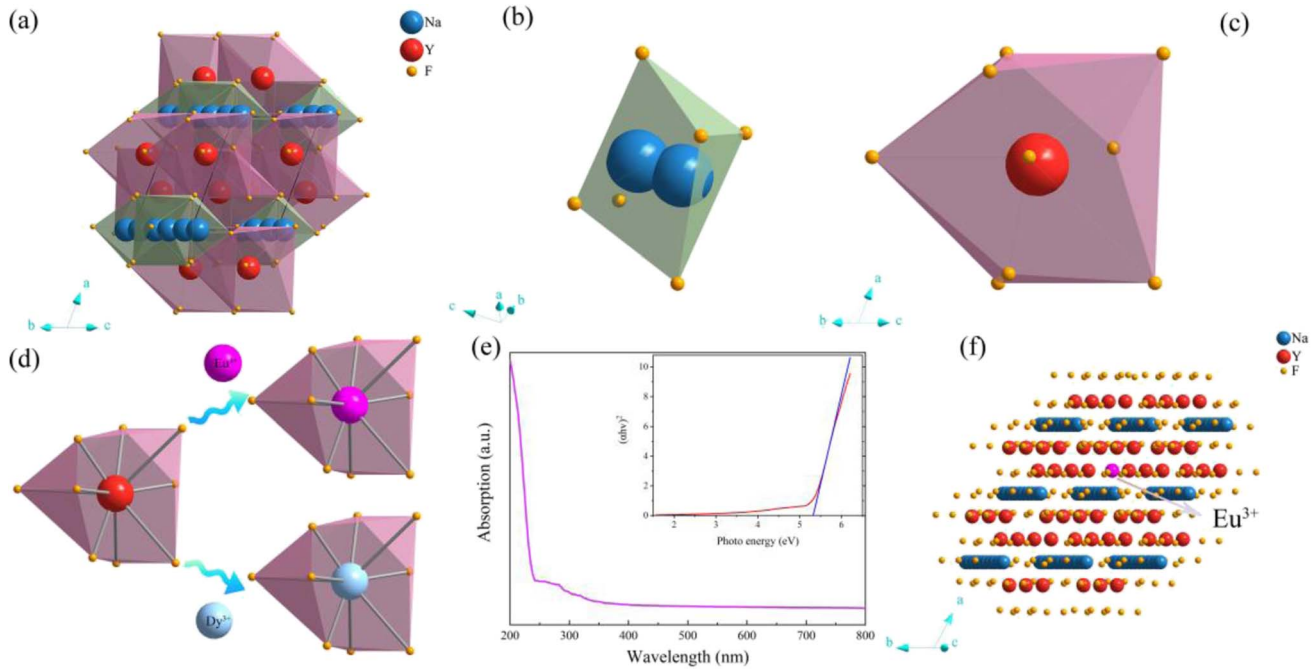

Fig. 5 (a) The crystal structure graph of β-$NaYF_4$. (b) Y–F decahedron. (c) Na–F octahedron. (d) The mechanism of incorporation of the Eu^{3+} and Dy^{3+} ions. (e) The ultraviolet visible absorption spectra of β-$NaYF_4$. (f) The crystal structure graph of β-$NaYF_4$0.065Eu^{3+} (2 × 2 × 2 supercell).

In this equation, α, h, and ν represent the absorption coefficient, Planck's constant, and frequency, respectively. A is a constant. E_g refers to the energy gap. n can be equal to 1/2 or 2, which represents the indirect or direct energy gap, respectively. In this study, n is chosen to be 1/2 (ref. 40). The energy gap of β-$NaYF_4$ is calculated to be 5.321 eV. A 2 × 2 × 2 supercell was built to illustrate the crystal structure model of β-$NaYF_4$: 0.065Eu^{3+} clearly. The crystal structure of β-$NaYF_4$: 0.065Eu^{3+} is shown in Fig. 5f, which demonstrates the crystal structure after incorporation of Eu^{3+}.

The band structure and density of states are portrayed in Fig. 6a and b, respectively. The band structure shows that the energy gap calculated by the DFT + U algorithm is 5.246 eV, which is slightly lower than the experimental result. According to Fig. 6b, the p-orbital of the Y element makes an enormous contribution for the deep energy level. For the conduction band, the s-orbital of Na is the predominant contributor. Otherwise, the p-orbital of the element Na forms a continued DOS in the range of −15 eV to −37 eV. Finally, the density of states located in the top of the valence band is supplied by the d-orbital of the element Y and the p-orbital of element F. Evidently, the large energy gap provides extraordinary circumstances for incorporation and transition of Eu^{3+} and Dy^{3+}, according to the results of the band structure and density of states.

3.4 Luminescence properties of β-$NaYF_4$: 0.065Eu^{3+},xDy^{3+}

As exhibited in Fig. 7a, the emission spectra of β-$NaYF_4$: 0.065Eu^{3+},xDy^{3+} (x = 0.001, 0.002, 0.003, 0.004, and 0.005), all samples present strong red-light emission. Otherwise, a main emission peak emerges at 615 nm, which could be ascribed to the $^5D_0 \rightarrow {}^7F_2$ transition. At a wavelength of 592 nm, orange-red light emission was detected, which contributed to the $^5D_0 \rightarrow {}^7F_2$ transition. According to the Judd–Ofelt theory,[41,42] the luminous intensity ratio of $^5D_0 \rightarrow {}^7F_2$ and $^5D_0 \rightarrow {}^7F_1$ ($R = I_2/I_1$) is a vital criterion to confirm the emission mode determined by the magnetic dipole (MD) transition ($^5D_0 \rightarrow {}^7F_2$) or electric dipole (ED) transition ($^5D_0 \rightarrow {}^7F_1$). When the R value is larger than 1, the emission mode would be determined by the ED transition. On the contrary, if the R value is smaller than 1, the emission mode would be determined by the MD transition. As the Dy^{3+}concentration increases, the R values of a series of β-$NaYF_4$: 0.065Eu^{3+},xDy^{3+} are 1.997, 1.983, 2.050, 2.049, 1.904, and 2.032, which suggests that the emission mode of all the samples are decided by the electric dipole (ED) transition.

As illustrated in Fig. 7a–c, the luminous intensities of a series of $NaYF_4$: 0.065Eu^{3+},xDy^{3+} increase in a range of concentration of Dy^{3+} from 0 to 0.03, a declining trend of emission intensity emerges when the concentration of Dy^{3+} exceeds 0.003. The luminous intensities of $NaYF_4$: 0,065Eu^{3+},xDy^{3+} (x = 0.001, 0.002, 0.003, 0.004, and 0.05) are 399.11%, 522.65%, 561.67%, 545.60%, and 492.45% of $NaYF_4$: 0,065Eu^{3+}, respectively. The results of the emission spectra indicate that concentration quenching occurs when the concentration of Dy^{3+} reaches 0.003. The optimal incorporating concentration of Dy^{3+} is 0.003. To elucidate the mechanism of quenching, eqn (2)[43] is utilized:

$$R_c = 2 \times (3V/4\pi x_c N)^{1/3} \quad (2)$$

where V, x_c, and N are equal to the crystal cell volume, concentration of sample corresponding to supreme luminous intensity, and the number of possible replacement sites of Eu^{3+} and Dy^{3+}, respectively. In this work, according to Table 1, V and N are equal to 109.228 and 6, while x_c is 0.068. The R_c value is

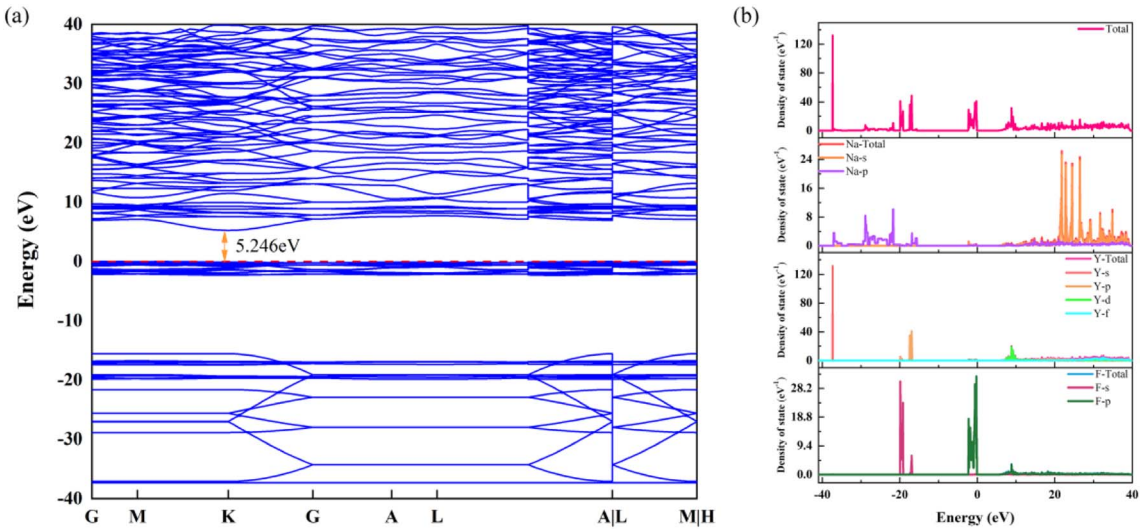

Fig. 6 (a) The band structure of β-$NaYF_4$. (b) The total and projected density of states of β-$NaYF_4$.

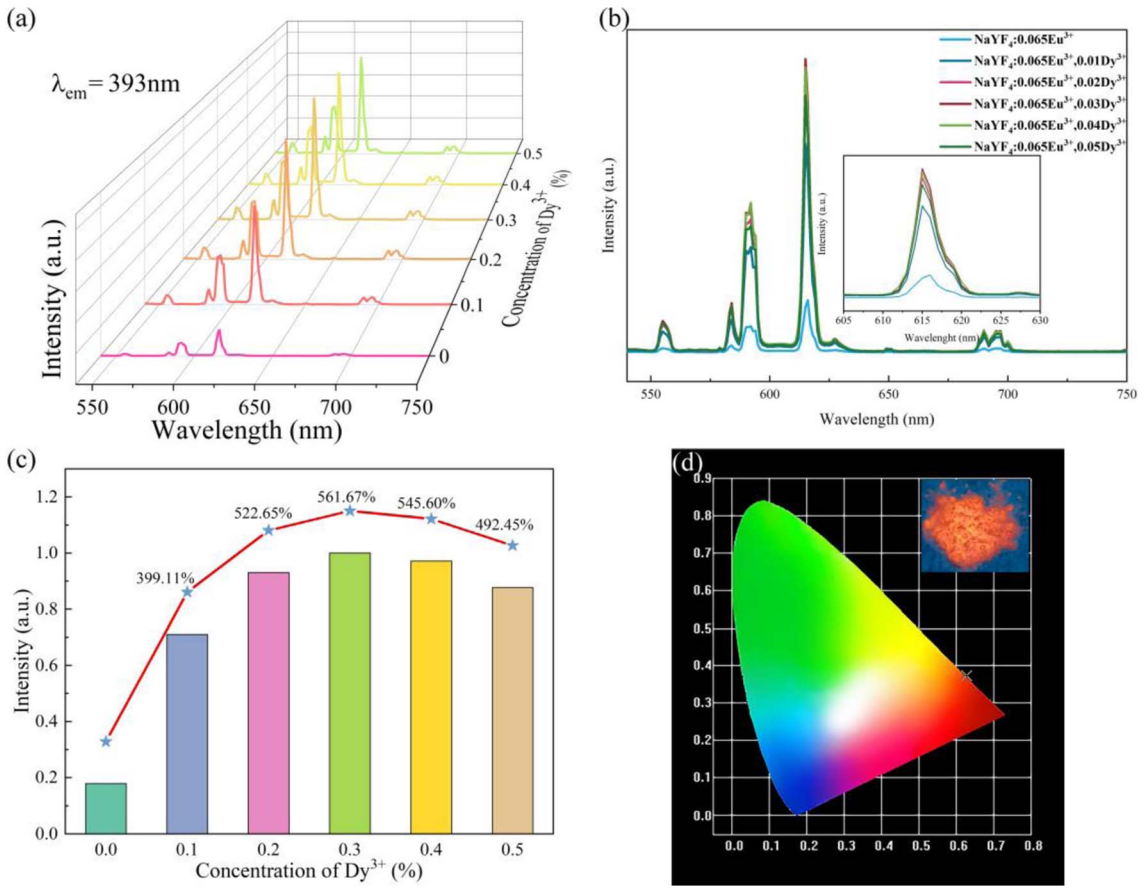

Fig. 7 (a) Emission spectra of samples incorporated with different concentrations of Dy^{3+}. (b) Emission spectra of samples incorporated with different concentrations of Dy^{3+} shown by a 2-dimensional graph. (c) Emission intensity of the major emission peak. (d) CIE chromaticity diagram and luminous photo of $NaYF_4$: $0.065Eu^{3+}$,$0.003Dy^{3+}$.

calculated to be 8.035, which is far away from 5 Å. The calculation results of the R_c value suggest that the electric multipolar interaction is the chief factor for concentration quenching. As illustrated in Fig. 7d, the sample $NaYF_4$: $0.065Eu^{3+}$,$0.003Dy^{3+}$ shows a brilliant orange-red emitting color under the excitation of a UV-lamp.

Table 2 Quantum yield and CIE coordinates of $NaYF_4$: $0.065Eu^{3+}$,xDy^{3+}

Sample	Quantum yield (%)	CIE coordinate x	CIE coordinate y
NaY_4 : $0.065Eu^{3+}$,$0.001Dy^{3+}$	64.65	0.6272	0.3724
NaY_4 : $0.065Eu^{3+}$,$0.002Dy^{3+}$	69.53	0.6263	0.3733
NaY_4 : $0.065Eu^{3+}$,$0.003Dy^{3+}$	77.49	0.626	0.3736
NaY_4 : $0.065Eu^{3+}$,$0.004Dy^{3+}$	73.02	0.6259	0.3737
NaY_4 : $0.065Eu^{3+}$,$0.005Dy^{3+}$	71.19	0.6251	0.3744

The quantum yield (QY) and CIE coordinates of $NaYF_4$: $0.065Eu^{3+}$,xDy^{3+} are listed in Table 2. The QY increases from 64.65% to 77.49% as the concentration of Dy^{3+} increases from 0.001 to 0.003. When the concentration of Dy^{3+} is 0.004 and 0.005, the QYs of those two samples are 73.02% and 71.19%, respectively. As the concentration of the Dy^{3+} ion increases, the CIE coordinates of x slightly decrease from 0.6272 to 0.6251, while the y value of the CIE coordinates increases from 0.3724 to 0.3744.

As demonstrated in Fig. 8a, the decay of all samples was measured at room temperature and fitted by the following equation:[44]

$$I_t = A_1 \exp\left(-\frac{t}{\tau_1}\right) + A_2 \exp\left(-\frac{t}{\tau_2}\right) + I_0 \quad (3)$$

where I_t and I_0 are the luminescence intensity at a selected time t and 0. A_1 and A_2 are constants and τ_1 and τ_2 are the brisk and unhurried time for decay constants, respectively. According to eqn (3), the average decay time is expressed as the following expression:

$$\tau = (A_1\tau_1^2 + A_2\tau_2^2) / (A_1\tau_1 + A_2\tau_2) \quad (4)$$

as the concentration of Dy^{3+} increases from 0 to 0.005, the lifetimes of the samples are fitted to be 6.63 ms, 6.48 ms, 6.48 ms, 6.08 ms, 5.99 ms, and 5.97 ms, respectively, indicating a decreasing trend with increasing concentration of Dy^{3+}, which can be ascribed to a poor impact stemming from concentration quenching. As shown in Fig. 8b, the lifetimes of Dy^{3+} in $NaYF_4$: $0.065Eu^{3+}$ were detected and are depicted. The lifetimes of Dy^{3+}incorporated into $NaYF_4$: $0.065Eu^{3+}$ are fitted to be 0.89 ms, 0.87 ms, 0.78 ms, 0.77 ms, and 0.72 ms, corresponding to concentrations of Dy^{3+} of 0.01, 0.02, 0.03, 0.04, and 0.05, respectively. The fitted results of decay demonstrate a linear decrease with the increase in the concentration of Dy^{3+}, suggesting the existence of energy transfer from Dy^{3+} to the Eu^{3+} ion. To calculate the efficiency of energy transfer, eqn (5)[45] is employed:

$$\eta_T = 1 - \frac{\tau}{\tau_0} \quad (5)$$

where τ and τ_0 are the decay of Dy^{3+} in the matrix with and without Eu^{3+}, respectively. As illustrated in Fig. 8c, when the Dy^{3+} was incorporated solely into the $NaYF_4$ matrix with a concentration range from 0.001 to 0.005, the lifetimes of Dy^{3+} were calculated to be 1.10 ms, 1.14 ms, 1.07 ms, 1.01 ms, and 1.00 ms, respectively. Hence, energy transfer efficiency can be calculated to be 19.09%, 23.68%, 27.10%, 23.76%, and 28.00%. An increasing trend is shown with the increasing concentration of Dy^{3+}. Despite the higher η_T of $NaYF_4$: $0.065Eu^{3+}$,$0.005Dy^{3+}$ than $NaYF_4$: $0.065Eu^{3+}$,$0.003Dy^{3+}$, the luminous intensity of the former is still lower than the latter due to the stronger concentration quenching effect.

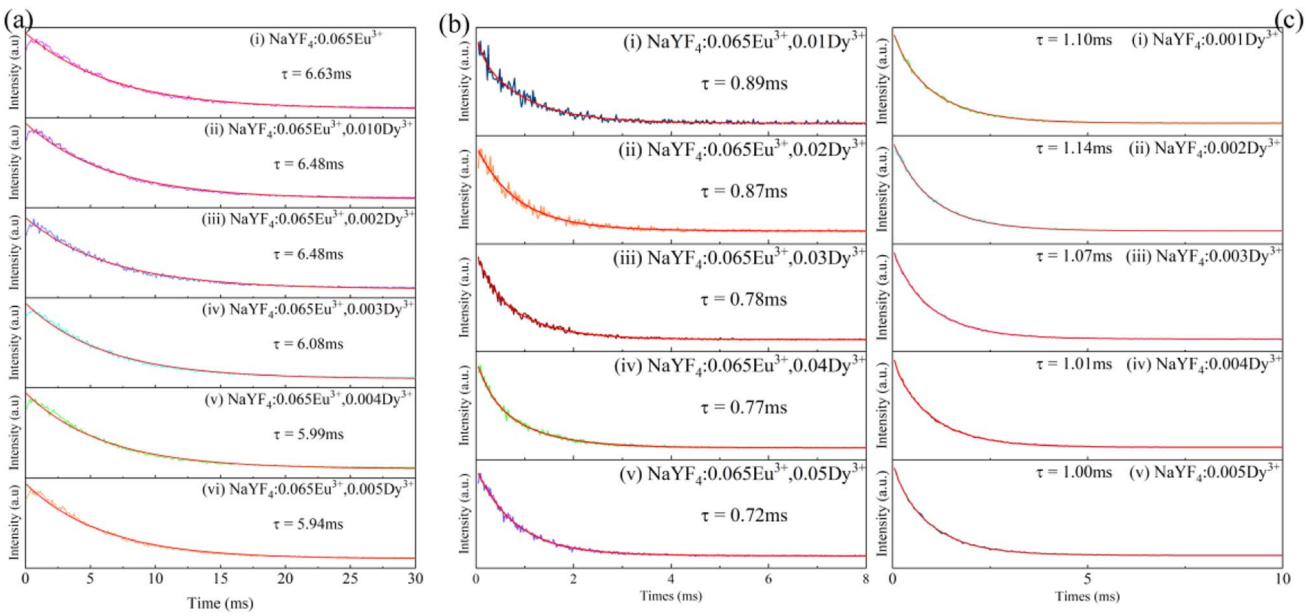

Fig. 8 (a) Decay of Eu^{3+} in $NaYF_4$: $0.065Eu^{3+}$,xDy^{3+}. (b) Decay of Dy^{3+} in $NaYF_4$: $0.065Eu^{3+}$. (c) Decay of Dy^{3+} in $NaYF_4$.

To elucidate the energy transfer mechanism, it is necessary to express the relationship between the luminous intensity and concentration of ions by a suitable method. The following equation[45] is utilized:

$$I_0/I \propto C^{n/3} \quad (6)$$

where I_0, I, and C represent the luminous intensity of the Dy^{3+}ion in the $NaYF_4$ matrix, the luminous intensity of Dy^{3+} in the $NaYF_4:0.065Eu^{3+}$ samples, and the total concentration of Dy^{3+} and Eu^{3+}, respectively. Otherwise, n can be equal to 6, 8, and 10 which represent the dipole–dipole, the dipole–quadrupole, and the quadrupole–quadrupole interactions.

The luminous intensity of Dy^{3+} in the absence and presence of Eu^{3+} was measured by emission spectra presented in Fig. 9a and b to acquire I_0 and I. The normalized intensities of I_0 and I are compared in Fig. 9c. It is remarkable that the changing trend for luminous intensity of Dy^{3+} is identical to the intensity of $NaYF_4:0.065Eu^{3+},xDy^{3+}$ excited by 393 nm. According to Fig. 9d that shows the fitted results of I_0/I and $C^{n/3}$, when the n value is equal to 8, the R^2 is the maximum value that equals 0.40286. The fitted result indicates that the energy transfer between Dy^{3+} and Eu^{3+} is ascribed to dipole–dipole interactions. Based on Fig. 9e–h, which show the excitation and emission spectra of Eu^{3+} and Dy^{3+}, the schematic diagram of energy transfer is portrayed in Fig. 9i. Under the excitation of 393 nm, electrons in the ground state of Eu^{3+} are excited to the excited state ($^5L_6$) and transition to $^4F_1$ and $^4F_2$ from $^5D_0$. Otherwise, the electrons in the ground state of Dy^{3+} are excited to the $^4I_{13/2}$ and $^4I_{15/2}$ energy level and transition to $^6H_{13/2}$ and $^6H_{15/2}$ from $^5F_{9/2}$. Due to the higher energy of $^5F_{9/2}$ compared to $^5D_0$, the electrons will transition from $^5F_{9/2}$ to the $^5D_0$ energy level, which will lead to energy transfer of Dy^{3+} to Eu^{3+}.

3.5 Thermal luminous properties of $NaYF_4:0.065Eu^{3+},0.003Dy^{3+}$

As depicted in Fig. 10a and b, under the excitement wavelength of 393 nm, the emission intensity of the sample demonstrates a linear increase in the temperature range from 303 K to 363 K. The luminous intensity of the sample was determined at 363 K and the optimal temperature for luminous intensity is 121.07%

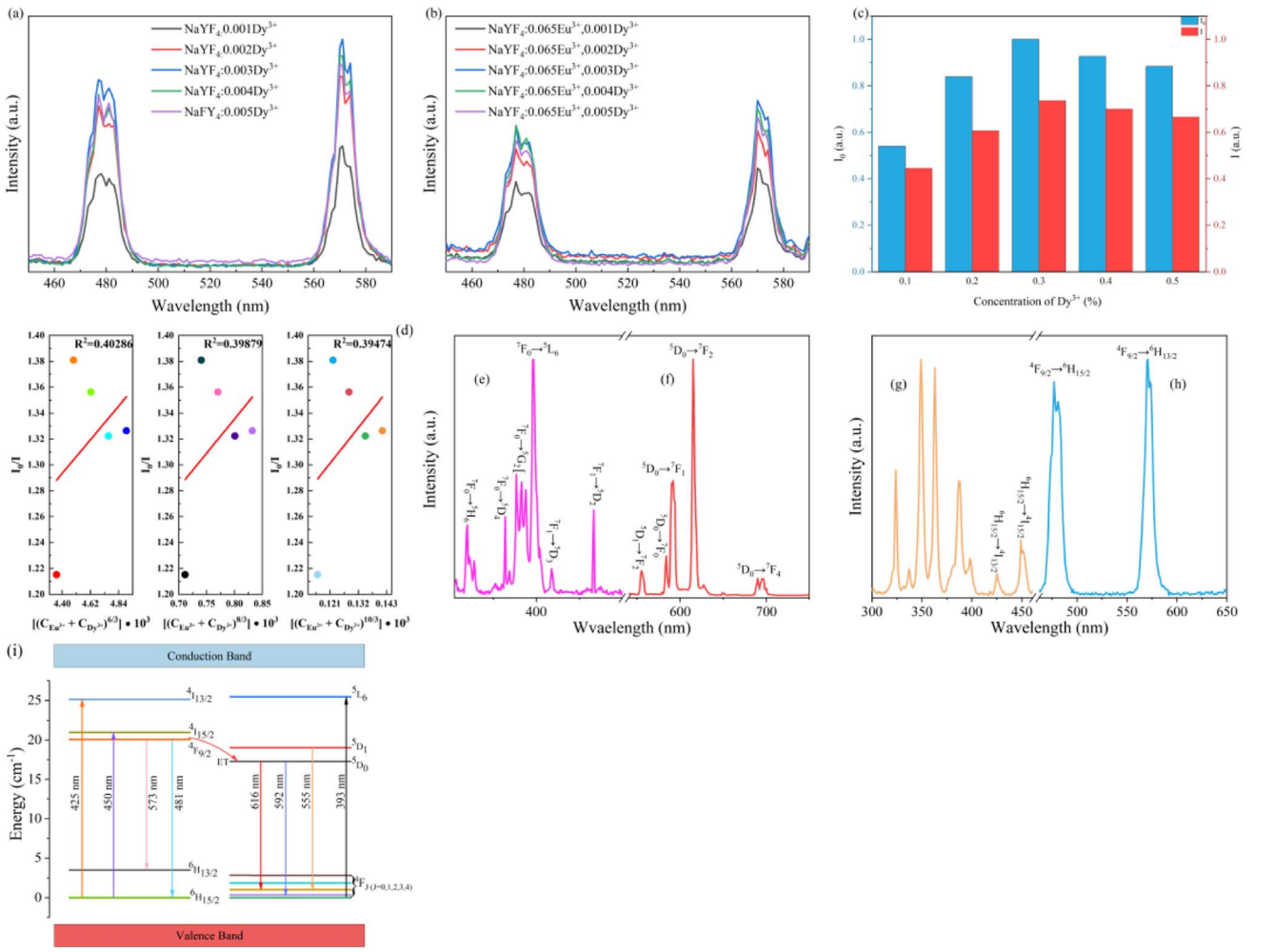

Fig. 9 (a) Emission spectra of $NaYF_4:xDy^{3+}$. (b) Emission spectra of Dy^{3+} in $NaYF_4:0.065Eu^{3+},xDy^{3+}$. (c) Values of I and I_0. (d) The fitted results of $n = 6$, $n = 8$, and $n = 10$. (e) Excitation spectra and (f) emission spectra of Eu^{3+} in $NaYF_4:0.065Eu^{3+},0.003Dy^{3+}$. (g) Excitation spectra and (h) Emission spectra of Dy^{3+} in $NaYF_4:0.065Eu^{3+},0.003Dy^{3+}$. (i) A schematic diagram of energy transfer from Dy^{3+} to Eu^{3+}.

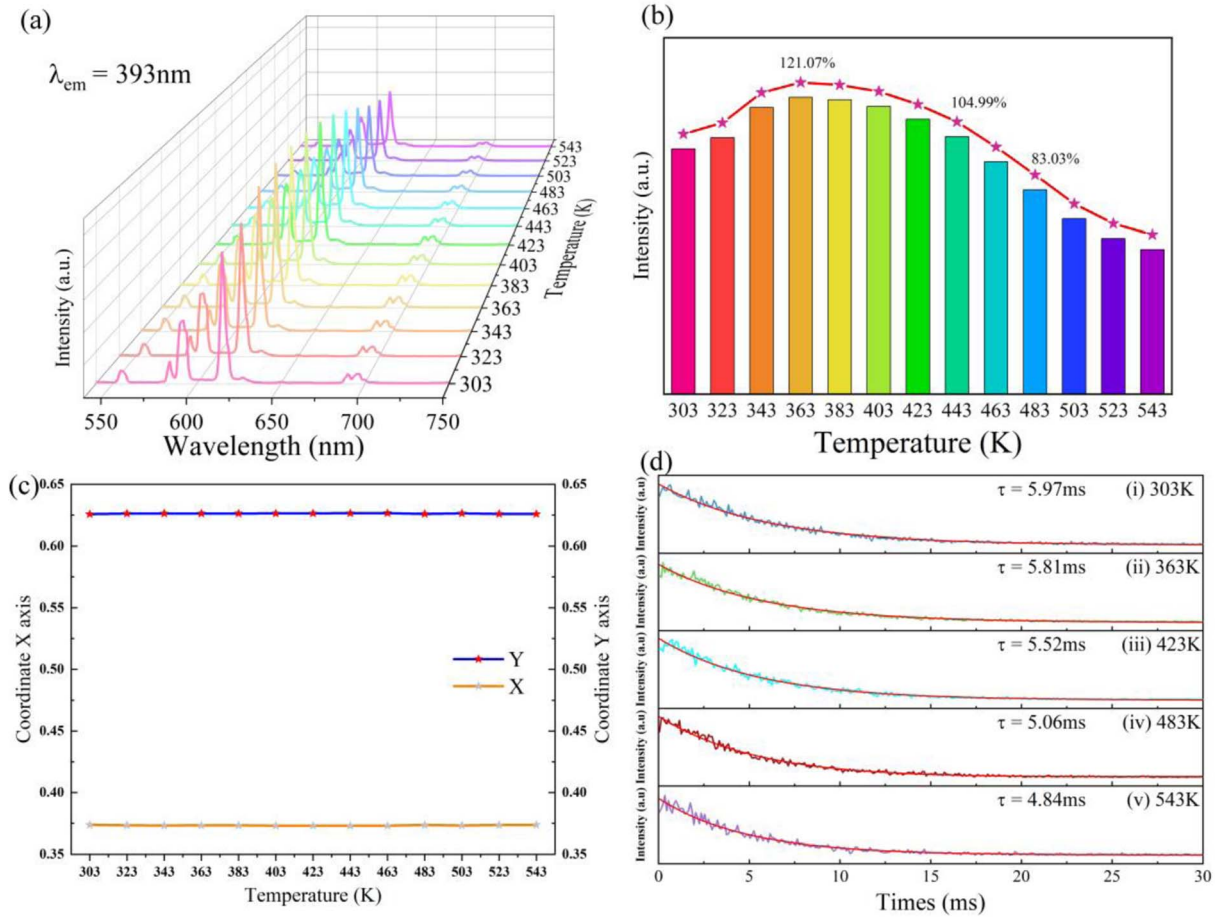

Fig. 10 (a) Emission spectrum of $NaYF_4$: $0.065Eu^{3+}$,$0.003Dy^{3+}$ at a distinct temperature. (b) Luminous intensity of the primary emission peak at temperatures 303 K to 543 K. (c) Change of CIE color coordinates from 303 K to 543 K. (d) Decay measured at 303 K, 363 K, 423 K, 483 K, and 543 K.

of intensity at 303 K. When the measurement temperature was higher than 363 K, the luminous intensity shows a linear decreasing trend. The luminous intensity measured at 443 K and 483 K remains 104.99% and 83.03% of luminous intensity at 303 K, respectively. There are not any additional emission peaks as measurement temperature increases. The shape of the emission spectra measured at high temperatures is identical to the spectra at room temperature. This result suggests that the sample of $NaYF_4$: $0.065Eu^{3+}$,$0.03Dy^{3+}$ presents outstanding thermal luminous performance. Based on the emission spectra measured at distinct temperatures, as illustrated in Fig. 10c, the change of CIE coordinate at different measurement temperatures shows a negligible change after 443 K. Before being heated to 443 K, the CIE coordinate in the temperature range from 323 K to 423 K can be considered as invariable, indicating the extraordinary red-light stability presented by the sample.

As portrayed in Fig. 10d, the decay measured at 303 K and 363 K indicates a slight decline from 5.97 ms to 5.81 ms which corresponds to increasing luminous intensity from 303 K to 363 K. A sharp decrease of decay from 5.52 ms to 4.84 ms represents the dwindling process of thermal luminous intensity led by the thermal quenching effect at a temperature range from 423 K to 543 K.

3.6 The zero thermal quenching mechanism of $NaYF_4$: $0.065Eu^{3+}$,$0.003Dy^{3+}$

The ZTQ performance presented by the sample can be ascribed to the crystal defect, as reported previously.[46,47] The source of the crystal defect should be taken into consideration. As illustrated in Fig. 3b and c, the high resolution XPS of Na and Y present two distinct chemical bonds of Na–F and Y–F, respectively. As Fig. 3b presents, two peaks are portrayed at 1070.95 eV and 1071.84 eV, which are close to 1071.4 eV [48] and 1072.5 eV,[49] corresponding to the standard binding energy of Na–F, respectively. As portrayed in Fig. 3c, the Y–F bond presents two kinds of binding energy, corresponding to 158.82 eV and 160.88 eV. Both those values are close to 159.10 eV [50] and 161.20 eV,[51] representing the standard binding energy of YF_3. The existence of the distinct chemical bonds of Na–F and Y–F is also confirmed by the crystal information listed in Table 1. The table presents two different occupancies for Na^+ and Y^{3+} ions. Combined with the result of X-ray refinement, nonequivalent replacement between Na^+ and Y^{3+} ions can be confirmed.

As shown in Fig. 11a, the Y^{3+} ion replaces the Na^+ ion inside the $[Na_2F_6]$ octahedron, which will produce a negative vacancy named V_Y'' and a cation vacancy $V_Y^{\cdot\cdot}$. Similarly, the Na^+ ion will replace the interior Y^{3+} ion of the $[YF_8]$ decahedrons, as

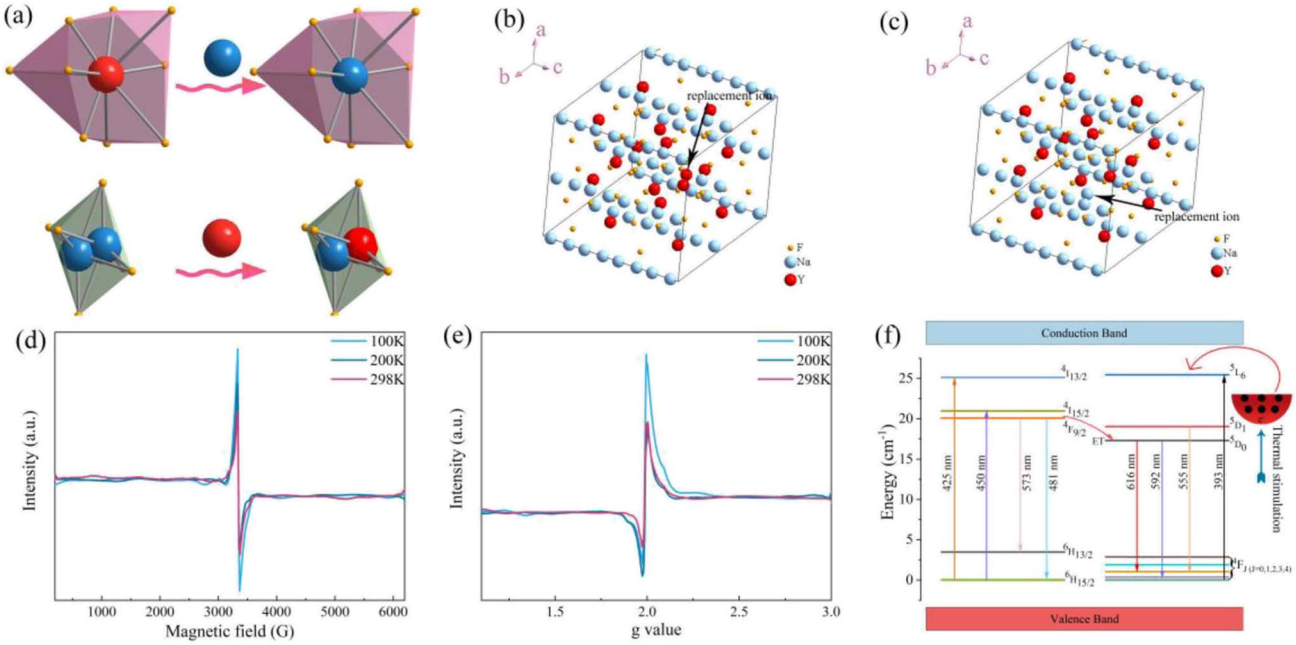

Fig. 11 (a) Replacement between Na^+ and Y^{3+}. (b) Calculation model for the V_Y vacancy. (c) Calculation model for the V_{Na} vacancy. (d) EPR spectra at 100 K, 200 K, and 298 K. (e) Calculated g values at 100 K, 200 K, and 298 K based on EPR spectra. (f) A zero thermal quenching mechanism schematic diagram of $NaYF_4$: $0.065Eu^{3+}$,$0.003Dy^{3+}$.

illustrated in Fig. 11a, which would introduce the negative vacancy V''_{Na} and the cation vacancy $V^{\cdot\cdot}_{Na}$. Two pairs of vacancies would be produced due to the requirement of electric neutrality for a whole crystal. A nonequivalent replacement process can be inferred and expressed by the following expression:

$$Y^{3+} + Na^+ \rightarrow V''_Y + V^{\cdot\cdot}_Y \quad (7)$$

$$Na^+ + Y^{3+} \rightarrow V''_{Na} + V^{\cdot\cdot}_{Na} \quad (8)$$

EPR, a well acknowledged method to characterize defects, was utilized for the purpose of characterizing crystal defects. The EPR signal was measured at 100 K, 200 K, and 298 K, as shown in Fig. 11b, manifesting a single kind of signal. The intensity of the signal decreases from 100 K to 298 K. Comparing the signal at 298 K with 200 K, the intensity of the signal shows a slight decline. The EPR signal was converted to a g value, which is a critical parameter for crystal defects, according to the following equation:[52]

$$g = 0.714477345 \times \frac{\nu}{B_0} \quad (9)$$

In this equation, the ν refers to the measurement frequency. B_0 represents the intensity of the magnetic field. As illustrated in Fig. 11c, the g value was calculated to be 1.9882, 1.9883, and 1.9878 at 100 K, 200 K, and 298 K, respectively. The calculated results clearly show the stable existence of crystal defects at room temperature. Furthermore, the sample keeps a stable g value at a distinct measurement temperature. Typical g values for the element Eu are 0.6134 and 1.3887, corresponding to ^{153}Eu and ^{151}Eu.[53] Similarly, representative g values for element Dy are 0.5122 and 0.7177, corresponding to ^{161}Dy and ^{163}Dy,[53] respectively. Those four values are far away from the calculated g values according to EPR, which suggests that the EPR signal does not stem from the unpaired electrons of elements Eu and Dy. It is confirmed that the crystal defect leads to the signal detected by EPR.

To further confirm the type of crystal defect, VASP was employed to calculated the formation energy of a defect. Eqn (10)[54] is necessary for the calculation:

$$E_f(\text{defect}) = E_t(\text{defect}) - E_t(\text{perfect}) - \left(\sum_i n_i \mu_i\right) + q(\varepsilon_{VBM} + \varepsilon_F) \quad (10)$$

where E_f (defect) refers to the formation energy of the defect. E_t (defect) and E_t (perfect) represent the total energy of a crystal with a present and absent defect, respectively. The n and μ correspond to the number of atoms and chemical potential of the element. The q is the charge state of the crystal defect. Finally, ε_{VBM} and ε_F are the maximum values of the valence band and the energy of Fermi level, respectively. The chemical potential of Na originates from the minimized total energy of Na ($P6_3/mmc$) divided by two Na atoms. Similarly, the chemical potential of Y and F originate from the minimum total energy of Y ($P6_3/mmc$) and F_2 ($P3/mn$) divided by two Y atoms and eight F atoms, respectively. The calculation model is presented in Fig. 11b and c.

Table 3, listing all the values of formation energy, suggests that the formation energy of V''_{Na} (−1310.7589 eV) and $V^{\cdot\cdot}_{Na}$ (−1267.5217 eV) is much higher than V''_Y (−43.2101 eV) and $V^{\cdot\cdot}_Y$ (18.2062 eV). The DFT calculation results demonstrate that the formation of V''_Y and $V^{\cdot\cdot}_Y$ vacancies will occur due to the

Table 3 Formation energy of the distinct defect

	V''_{Na}	$V^{\cdot}_{Na}$	V''_{Y}	$V^{\cdot}_{Y}$
E_t (perfect)	−426.2295	−426.2295	−426.2295	−426.2295
E_t (defect)	−1724.1516	−1732.7422	−449.95187	−440.36326
ε_{VBM}	7.6929	7.6929	7.6929	7.6929
ε_F	5.246	5.246	5.246	5.246
$\sum n_i\mu_i$	−13.0771	−13.0771	−6.4261	−6.4261
E_f (defect)	−1310.7589	−1267.5217	−43.2101	18.2062

requirement for electrons to balance, rather and V''_{Na} and $V^{\cdot}_{Na}$. Furthermore, V''_{Na} and $V^{\cdot}_{Na}$ will be hard to produce due to the high formation energy, despite the nonequivalent replacement between Na^+ and Y^{3+} located in the $[YF_8]$ decahedron.

On the other hand, the crystal defect plays the vital role of the electron trap.[55,56] Based on this property, unpaired electrons induced by nonequivalent replacement are captured by the electron trap to maintain the electric neutrality of the whole system. Combining the EPR spectra, V''_{Y} and $V^{\cdot}_{Y}$ vacancies show a single signal in Fig. 11a and b, due to the identical chemistry environment of the two types of vacancies. The expression expressing the formation of crystal defect should be modified as the following:

$$Y^{3+} + Na^{+} \rightarrow V''_{Y} + V^{\cdot}_{Y} \quad (11)$$

Based on the analysis of EPR and DFT calculations, V''_{Y} and $V^{\cdot}_{Y}$ vacancies, treated as electronic traps, make a predominant contribution to the zero thermal quenching performance of $NaYF_4:0.065Eu^{3+},0.003Dy^{3+}$. As illustrated in Fig. 11f, with an increase of temperature, under thermal stimulation, electrons caught in electronic traps will be excited to the $^5L_6$ energy level

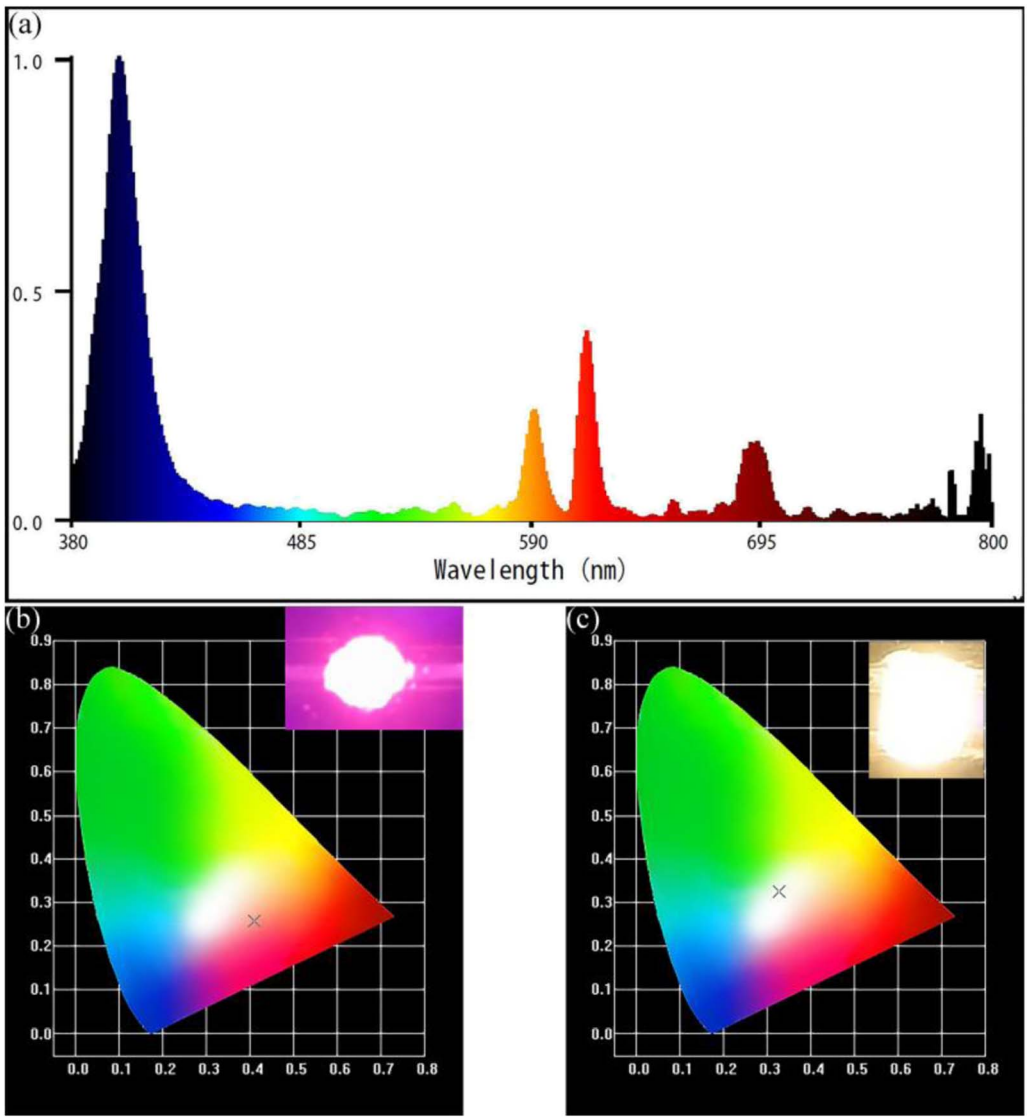

Fig. 12 (a) Luminescent performance of prototype LEDs ($NaYF_4:0.065Eu^{3+},0.003Dy^{3+}$ + 395 nm UV chip) and luminescent graph. (b) The CIE chromaticity diagram of fabricated LEDs. (c) The CIE coordinate and fabricated WLEDs combining the YAG : Ce^{3+} yellow phosphor with $NaYF_4$: $0.065Eu^{3+},0.003Dy^{3+}$ phosphor and 395 nm UV chip.

and transition to ^4F_J ($J = 0, 1, 2, 3, 4$) level, to compensate for the loss of luminous intensity induced by thermal quenching. In the temperature range of 303 K to 363 K, the luminous intensity increases linearly due to the increasing number of excited electrons stored in electronic traps, corresponding to the stage of increasing luminous intensity. This process is presented by the lifetimes measured at 303 K and 363 K. Comparing the decay times of 363 K with 303 K, the lifetimes decrease by 2.68%, while the decay at 423 K, 483 K, and 543 K declines by 7.82%, 14.572%, and 18.972%, respectively. The change of decay time shows the evident compensation effect induced by electrons in defects at 303 K to 363 K. After heating to 386 K, the luminous intensity begins to decline due to the decreasing number of excited electrons in electronic traps. Noticeably, the thermal luminous intensities remain 104.99% and 83.03% at 443 K and 483 K, respectively. The $NaYF_4:0.065Eu^{3+},0.003Dy^{3+}$ red-light phosphor demonstrates extraordinary thermal luminous properties.

3.7 Fabrication of the prototype red light LED

As shown in Fig. 12a, the prototype red LED was fabricated by coating the $NaYF_4:0.065Eu^{3+},0.003Dy^{3+}$ phosphor onto the surface of the 395 nm UV-chip. The red light ratio reached 35.4% under the 9 mA driving current, indicating the extraordinary red-light performance of the $NaYF_4:0.065Eu^{3+},0.003Dy^{3+}$ red-light phosphor. A white light emitting diode was fabricated by combining the $YAG:Ce^{3+}$ yellow phosphor with the $NaYF_4:0.065Eu^{3+},0.003Dy^{3+}$ phosphor and 395 nm UV chip. Under a current of 9 mA, the correlated color temperature and color-rendering index of this fabricated WLED are 5698 K and 82.2, respectively. The CIE coordinate of the fabricated WLED is $(x, y) = (0.3284, 0.3243)$, which is the white light area. The result shows that $NaYF_4:0.065Eu^{3+},0.003Dy^{3+}$ has outstanding thermal stability and the red-light source is an extraordinary candidate for WLEDs. Fig. 12b shows the color region of the prototype LED in the CIE chromaticity diagram, unveiling a close color area to white light. This result provides powerful proof that the $NaYF_4:0.065Eu^{3+},0.003Dy^{3+}$ phosphor is an ideal red-light component for WLEDs.

4. Conclusions

A series of $NaYF_4:0.065Eu^{3+},xDy^{3+}$ ($x = 0.001$, 0.002, 0.003, 0.004, 0.005) red-light phosphors were synthesized by a one-step hydrothermal method. The energy transfer effect was determined to be due to dipole–quadrupole interactions. With the increasing concentration of Dy^{3+}, the luminous intensity of β-$NaYF_4:0.065Eu^{3+},xDy^{3+}$ is 399.11%, 522.65%, 561.67%, 545.60%, and 492.45% of $NaYF_4:0{,}065Eu^{3+}$, respectively. The zero thermal quenching property of the $NaYF_4:0.065Eu^{3+},0.003Dy^{3+}$ phosphor can be ascribed to the thermal stimulation of electrons stored in the crystal defect which is treated as an electronic trap. DFT calculations were employed to elucidate that V_Y'' and $V_Y^{\cdot\cdot}$ vacancies are predominant in the crystal and lead to the zero thermal quenching property. The formation energy of the V_Y'' and $V_Y^{\cdot\cdot}$ vacancies was calculated to be −43.2101 eV and 18.2062 eV, respectively.

Conflicts of interest

The authors declare that they have no known competing financial interests or personal relationships that could have appeared to influence the work reported in this paper.

Acknowledgements

This research is supported by the National Natural Science Foundation of China (Grant No. 21661006 and No. 21965004), the Natural Science Foundation of Guangxi Zhuang Autonomous Region, China (Grant No. 2019GXNSFDA245022, No. 2020GXNSFAA159036), the Scientific Research Foundation of Guangxi University (Grant No. XDZ140116), the innovation Project of Guangxi Graduate Education (Grant No. YCSW2020015), and the Students Experimental Skills and Innovation Ability Training Fund Project of Guangxi University (No. S202210593143). The calculation part was supported by the high performance calculation center of Guangxi University.

References

1 S. Liang, P. Dang, G. Li, M. S. Molokeev, Y. Wei, Y. Wei, H. Lian, M. Shang, A. A. Al Kheraif and J. Lin, *J. Mater. Chem. C*, 2018, **6**, 6714–6725.
2 S. Pimputkar, J. S. Speck, S. P. DenBaars and S. Nakamura, *Nat. Photonics*, 2009, **3**, 180–182.
3 E. F. Schubert and J. K. Kim, *Science*, 2005, **308**, 1274–1278.
4 P. M. Pattison, J. Y. Tsao, G. C. Brainard and B. Bugbee, *Nature*, 2018, **563**, 493–500.
5 R. J. Bula, R. C. Morrow, T. W. Tibbitts, D. J. Barta, R. W. Ignatius and T. S. Martin, *HortScience*, 1991, **26**, 203–205.
6 C. Kubota, T. Eguchi and M. Kroggel, *Sci. Hortic.*, 2017, **226**, 366–371.
7 S. A. Rahman, M. A. St Hilaire and S. W. Lockley, *Physiol. Behav.*, 2017, **177**, 221–229.
8 J. Chang, D.-s. Yang, Z.-h. Sun, Z.-c. Weng, H.-l. Jiang and T. Ren, *Chin. J. Lumin.*, 2008, **29**, 195–199.
9 J. W. Liu, G. Wang, L. Ma, K. L. Zhang, L. L. Zhang, Q. J. Wang and L. F. Wan, East China Normal University, Shanghai, Peoples R China, 2007.
10 Z. Xia and Q. Liu, *Prog. Mater. Sci.*, 2016, **84**, 59–117.
11 Z. Zhang, C. Ma, R. Gautier, M. S. Molokeev, Q. Liu and Z. Xia, *Adv. Funct. Mater.*, 2018, **28**, 1804150.
12 H. Liu, Y. Luo, Z. Mao, L. Liao and Z. Xia, *J. Mater. Chem. C*, 2014, **2**, 1619–1627.
13 W. Lu, M. Jiao, B. Shao, L. Zhao and H. You, *Inorg. Chem.*, 2015, **54**, 9060–9065.
14 L. Chen, C.-C. Lin, C.-W. Yeh and R.-S. Liu, *Materials*, 2010, **3**, 2172–2195.
15 C. C. Lin and R. S. Liu, *J. Phys. Chem. Lett.*, 2011, **2**, 1268–1277.
16 J. Ueda, P. Dorenbos, A. J. J. Bos, A. Meijerink and S. Tanabe, *J. Phys. Chem. C*, 2015, **119**, 25003–25008.

17 P. Pust, V. Weiler, C. Hecht, A. Tucks, A. S. Wochnik, A. K. Henss, D. Wiechert, C. Scheu, P. J. Schmidt and W. Schnick, *Nat. Mater.*, 2014, **13**, 891–896.
18 Q. Wei, J. Ding and Y. Wang, *Chem. Eng. J.*, 2020, **386**, 124004.
19 K. Binnemans, *Coord. Chem. Rev.*, 2015, **295**, 1–45.
20 H. Peng, H. Song, B. Chen, J. Wang, S. Lu, X. Kong and J. Zhang, *J. Chem. Phys.*, 2003, **118**, 3277–3282.
21 Y. Zhou, Z. Song, Y. Li, Q. Liu, Z. Xu, R. Hu, X. Zhang, J. Qiu and Z. Yang, *J. Rare Earths*, 2016, **34**, 1188–1192.
22 H. Zhu, C. C. Lin, W. Luo, S. Shu, Z. Liu, Y. Liu, J. Kong, E. Ma, Y. Cao, R. S. Liu and X. Chen, *Nat. Commun.*, 2014, **5**, 4312.
23 F. Tang, Z. Su, H. Ye, W. Gao, X. Pan and S. Xu, *ACS Omega*, 2018, **3**, 13704–13710.
24 H.-X. Mai, Y.-W. Zhang, R. Si, Z.-G. Yan, L.-D. Sun, L.-P. You and C.-H. Yan, *J. Am. Chem. Soc.*, 2006, **128**, 6426–6436.
25 J. W. Stouwdam and F. van Veggel, *Nano Lett.*, 2002, **2**, 733–737.
26 F. Vetrone, V. Mahalingam and J. A. Capobianco, *Chem. Mater.*, 2009, **21**, 1847–1851.
27 L. Mao, Z. Lu, N. He, L. Zhang, Y. Deng and D. Duan, *Sci. China: Chem.*, 2016, **60**, 157–162.
28 B. Dong, H. W. Song, H. Q. Yu, H. Zhang, R. F. Qin, X. Bai, G. H. Pan, S. Z. Lu, F. Wang, L. B. Fan and Q. L. Dai, *J. Phys. Chem. C*, 2008, **112**, 1435–1440.
29 H. X. Mai, Y. W. Zhang, R. Si, Z. G. Yan, L. D. Sun, L. P. You and C. H. Yan, *J. Am. Chem. Soc.*, 2006, **128**, 6426–6436.
30 G. S. Yi, H. C. Lu, S. Y. Zhao, G. Yue, W. J. Yang, D. P. Chen and L. H. Guo, *Nano Lett.*, 2004, **4**, 2191–2196.
31 M. Calil Júnior, Á. Melo, E. Rodrigues, F. Sigoli and M. Rodrigues, *J. Braz. Chem. Soc.*, 2017, **28**, 1816–1821.
32 X. P. Chen, Q. Y. Zhang, C. H. Yang, D. D. Chen and C. Zhao, *Spectrochim. Acta, Part A*, 2009, **74**, 441–445.
33 Y. Luo, R. Yang, X. Zhang, B. Hu, S. Hu, L. Zhou and J. Yang, *CrystEngComm*, 2015, **17**, 7762–7771.
34 X. Zhang, H. Zou, C. Xu, Z. An, R. Dong, K. Zheng, Y. Sheng and Y. Song, *Opt. Mater.*, 2019, **89**, 512–520.
35 A. R. Kadam and S. J. Dhoble, *J. Alloys Compd.*, 2021, **884**, 161138.
36 Z. Wang, L. Cheng, H. Tang, X. Yu, J. Xie, X. Mi, Q. Liu and X. Zhang, *J. Solid State Chem.*, 2021, **301**, 122295.
37 Q. Han, A. Hao, W. Gao, J. Qi, Y. Wang and J. Dong, *Ceram. Int.*, 2020, **46**, 11132–11136.
38 X. Wang, S. Zhao, Y. Zhang and G. Sheng, *J. Rare Earths*, 2010, **28**, 222–224.
39 V. Wang, N. Xu, J.-C. Liu, G. Tang and W.-T. Geng, *Comput. Phys. Commun.*, 2021, **267**, 108033.
40 M. G. Brik, A. M. Srivastava and A. I. Popov, *Opt. Mater.*, 2022, **127**, 112276.
41 B. R. Judd, *Phys. Rev.*, 1962, **127**, 750–761.
42 G. S. Ofelt, *J. Chem. Phys.*, 1962, **37**, 511–520.
43 Y. Sato, H. Kato, M. Kobayashi, T. Masaki, D. H. Yoon and M. Kakihana, *Angew. Chem., Int. Ed. Engl.*, 2014, **53**, 7756–7759.
44 K. Li, J. Fan, M. Shang, H. Lian and J. Lin, *J. Mater. Chem. C*, 2015, **3**, 9989–9998.
45 C. Cao, H. K. Yang, J. W. Chung, B. K. Moon, B. C. Choi, J. H. Jeong and K. H. Kim, *J. Mater. Chem.*, 2011, **21**, 10342–10347.
46 J. Tian and W. Zhuang, *Inorg. Chem. Front.*, 2021, **8**, 4933–4954.
47 X. Wang, Z. Zhao, Q. Wu, C. Wang, Q. Wang, L. Yanyan and Y. Wang, *J. Mater. Chem. C*, 2016, **4**, 8795–8801.
48 V. I. Nefedov, Y. V. Salyn, G. Leonhardt and R. Scheibe, *J. Electron Spectrosc. Relat. Phenom.*, 1977, **10**, 121–124.
49 H. Seyama, *J. Chem. Soc., Faraday Trans. 1*, 1985, **81**, 485–495.
50 R. P. Vasquez, M. C. Foote and B. D. Hunt, *J. Appl. Phys.*, 1989, **66**, 4866–4877.
51 U. Yoshinori, T. Akira, I. Toshio and Y. Hideo, *Bull. Chem. Soc. Jpn.*, 1986, **59**, 2263–2267.
52 K. Ye, K. Li, Y. Lu, Z. Guo, N. Ni, H. Liu, Y. Huang, H. Ji and P. Wang, *TrAC, Trends Anal. Chem.*, 2019, **116**, 102–108.
53 J. R. B. J. A. Weil, *Electron Paramagnetic Resonance: Elementary Theory Electron and Practical applications*, John Wiley & Sons, Hoboken, 2nd edn, 2007.
54 L. Jia, M. Gu, G. Song and J. Zhu, *Opt. Mater.*, 2019, **93**, 15–18.
55 S. Fang, T. Lang, T. Han, J. Wang, J. Yang, S. Cao, L. Peng, B. Liu, A. N. Yakovlev and V. I. Korepanov, *Chem. Eng. J.*, 2020, **389**, 124297.
56 G. Zhu, Z. Li, C. Wang, X. Wang, F. Zhou, M. Gao, S. Xin and Y. Wang, *Dalton Trans.*, 2019, **48**, 1624–1632.